Acta Materialia 292 (2025) 121017

Contents lists available at ScienceDirect

Acta Materialia

journal homepage: www.elsevier.com/locate/actamat

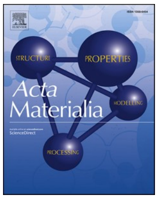

Revealing solidification behaviour and phase transformations in $Fe_{60}Co_{25}Ni_{10}Mo_5$ and $Fe_{63}Co_{26}Ni_{11}$ alloys by using high-speed video and *in situ* X-ray diffraction

Shilei Liu [a], Victoria Kaban [a], Olof Gutowski [b], Thomas Volkmann [c], Kornelius Nielsch [a,d], Ivan Kaban [a,*]

[a] *Leibniz Institute for Solid State and Materials Research Dresden, Helmholtzstraße 20, Dresden 01069, Germany*
[b] *Deutsches Elektronen-Synchrotron DESY, Notkestraße 85, Hamburg 22607, Germany*
[c] *Institut für Materialphysik im Weltraum, Deutsches Zentrum für Luft- und Raumfahrt (DLR), Linder Höhe, Köln 51147, Germany*
[d] *Institute of Materials Science, Technische Universität Dresden, Dresden 01062, Germany*

ARTICLE INFO

Keywords:
Undercooled melts
Solidification
High-speed video
Synchrotron X-ray diffraction
Phase transformations
Microstructure

ABSTRACT

A combination of time-resolved synchrotron X-ray diffraction (XRD), high-speed video and electromagnetic levitation (EML) enabled revealing the solidification path and phase transformations in $Fe_{60}Co_{25}Ni_{10}Mo_5$ and $Fe_{63}Co_{26}Ni_{11}$ alloys during heating and cooling. High-speed XRD provided direct evidence for nucleation of metastable δ-ferrite in undercooled liquid state and its quick transformation to γ-austenite. Addition of Mo clearly favours nucleation of δ-ferrite in $Fe_{60}Co_{25}Ni_{10}Mo_5$ melts undercooled by ΔT of about 100 K and more. In contrast, primary crystallisation of any of δ and γ phases appears to be possible in $Fe_{63}Co_{26}Ni_{11}$ melts at all levels of undercooling. Neither Ni nor Mo exhibit any notable effect on the growth behaviour of δ and γ phases, which remains close to the one in the $Fe_{60}Co_{40}$ base alloy. Alloying with Mo has a strong impact on the microstructure and solid state transformations in the $Fe_{60}Co_{25}Ni_{10}Mo_5$ samples such as grain refinement at $\Delta T < 200$ K, incomplete transformation of γ-austenite to α-ferrite, and formation of martensite at $\Delta T \geq 330$ K.

1. Introduction

Following the introduction of high-entropy alloys (HEAs) in 2004 [1, 2], multi-principal element alloys (MPEAs) and complex concentrated alloys (CCAs) have attracted significant attention. Being not limited by equiatomic concentrations, quantity of phases or magnitude of entropy, concepts of MPEAs and CCAs offer a new paradigm in alloy design [3–9]. High interest to these alloys is primarily driven by extended possibilities for tailoring the structural and functional properties, although high cost due to large concentrations of often quite expensive constituents remains an issue.

Recently, Kwon et al. [10] proposed the $Fe_{60}Co_{25}Ni_{10}Mo_5$ (at.%) maraging alloy, exhibiting ultra-high yield strength and strain hardening in tensile tests. The excellent mechanical properties have been obtained by creating the microstructure consisting of austenite, martensite and Mo-rich nanoprecipitates. Considering the application potential of $Fe_{60}Co_{25}Ni_{10}Mo_5$ alloy, it is worth to explore its solidification, phase constitution and phase transformations in detail. This is also interesting from a fundamental point of view since this composition could be considered as a derivative of the binary $Fe_{60}Co_{40}$ (at.%) alloy. The latter has been found to exhibit nucleation and growth competition between stable γ phase (austenite, face centred cubic structure – fcc) and metastable δ phase (ferrite, body centred cubic structure – bcc) while solidifying from undercooled liquid state [11–16].

The reports on primary solidification of δ phase and its subsequent transformation to γ in Fe-based alloys, e.g. Fe-Co [11–16], Fe-Ni [16–19], Fe-Cr-Ni [16,20–22], have been made on the base of microstructure analysis of rapidly quenched samples, high-speed pyrometry data and video observations. A direct evidence on δ→γ transformation has been provided by Shuleshova et al. [23] for $Fe_{80}Co_{20}$ (at.%) and Matson et al. [24] for $Fe_{72}Cr_{16}Ni_{12}$ (wt.%) by combining electromagnetic levitation (EML) and *in situ* high-energy X-ray diffraction (XRD) at the German Electron Synchrotron DESY, Hamburg. This was possible due to a relatively large delay time τ (order of seconds) between nucleation of the two phases. In contrast, δ phase could not be registered by *in situ* XRD for CrFeNi, CoCrNi and CoCrFeNi medium- and

---

* Corresponding author.
E-mail address: i.kaban@ifw-dresden.de (I. Kaban).

https://doi.org/10.1016/j.actamat.2025.121017
Received 18 November 2024; Received in revised form 28 March 2025; Accepted 4 April 2025

high-entropy alloys because the delay time was three orders of magnitude smaller [25].

In this work, we have studied solidification behaviour and phase transformations by using high-speed video camera running at 30,000 frames per second and photon counting X-ray detector taking up to 1000 patterns per second. It enabled recording the phase competition during near-equilibrium and non-equilibrium solidification of $Fe_{60}Co_{25}Ni_{10}Mo_5$ and $Fe_{63}Co_{26}Ni_{11}$ alloys as well as phase transformations occurring upon heating and cooling in solid state. The ternary composition has been chosen in order to clarify the role of Ni and Mo when added to the base $Fe_{60}Co_{40}$ alloy. The thermal properties and microstructure of the as-cast and EML processed samples have been analysed by using differential scanning calorimetry (DSC), XRD phase analysis, scanning electron microscopy (SEM), energy-dispersive X-ray spectroscopy (EDS) and electron backscatter diffraction (EBSD).

2. Materials and experimental procedures

$Fe_{60}Co_{25}Ni_{10}Mo_5$, $Fe_{63}Co_{26}Ni_{11}$ and $Fe_{60}Co_{40}$ master alloys (at.%) have been prepared from high-pure (99.99 wt.%) Fe, Co, Ni and Mo elements under Ar atmosphere by using an arc melter from Edmund Bühler. To ensure alloy homogeneity, each ingot was melted and solidified five times with inverting in-between. At the last stage, the melt was suction-cast into a Cu mould attached to a Cu hearth at the bottom. The obtained rods (6 mm diameter, 80 mm length) were ground with SiC paper up to P4000 grit and cut into cylindrical samples of about 1.2 g weight for the solidification studies. Cutting has been done by using an Accutom 50 machine from Struers. These samples were similarly ground on circular faces and cleaned in an ultrasonic bath with Ethanol for 10 min. This way it was possible to significantly reduce the appearance of oxides on the surface of molten samples during processing in the EML facility.

Slices with the thickness of approx. 0.5 mm were cut out from the as-cast rods for the XRD phase analysis. The measurements have been carried out in Bragg-Brentano geometry by using an X'Pert Pro X-ray diffractometer with Co-K_α radiation from PANalytical. The XRD intensities have been analysed by using the HighScore Plus software from PANalytical [26] and ICDD PDF-5+ data base [27].

Thermal analysis has been carried out by using the differential scanning calorimeter DSC 404 C from Netzsch. Specimens of 10–15 mg weight taken from the as-cast rods have been investigated during heating and cooling at a rate of 20 $K\cdot min^{-1}$ under Ar gas flow.

Solidification studies have been carried out by using the electromagnetic levitation (EML) facility at Leibniz IFW Dresden [23]. The samples were processed in a high-vacuum chamber which was preliminary evacuated to below $5\cdot 10^{-6}$ mbar rest air pressure and backfilled with high purity He (6 N) to 600 mbar. The induction coil used for levitation and heating of samples was powered by the high-frequency generator TruHeat HF 3010 from Hüttinger Elektronik. Cooling was realised by decreasing the electric current in the coil and applying two He jets blown onto a sample from opposite sides. The solidification was recorded at a rate of 30,000 frames per second with a high-speed video (HSV) camera FASTCAM SA5 775K-M3 from Photron. Spatial calibration of the HSV digital images was performed by using an image taken from a Ti-6Al-4V sphere of known size which was levitated at 1148 K. The images were analysed by using ImageJ software [28].

The temperature of levitated samples was measured with an optical pyrometer from Dr. Mergenthaler which was focused on the top of the sample. The pyrometer was operated in a single wave mode in the spectral range of 1.65–2 μm. In experiments at IFW Dresden, the pyrometer data were saved with a 50 Hz frequency. As the emissivity of alloys was not known, the temperature T^{pyro} was measured with $\varepsilon = 0.25$ and corrected by using the liquidus temperature from DSC as a reference. The correction has been done according to Eq. (1) which follows from Wien's law [29]

$$\frac{1}{T} = \frac{1}{T^{\mathrm{pyro}}} + \left(\frac{1}{T_{\mathrm{l}}^{\mathrm{DSC}}} - \frac{1}{T_{\mathrm{l}}^{\mathrm{pyro}}}\right), \quad (1)$$

where $T_{\mathrm{l}}^{\mathrm{DSC}}$ is the liquidus temperature measured by calorimeter and $T_{\mathrm{l}}^{\mathrm{pyro}}$ is a pyrometer reading. The melt undercooling ΔT was calculated as the difference between the liquidus temperature T_{l} and apparent nucleation temperature T_{n} determined by the lowest point on corrected $T(t)$ curve before recalescence. Considering the systematic and statistical uncertainties of the pyrometer and calorimeter, the total uncertainty of T_{l} and T_{n} was estimated to be ±7 K and ±3 K, respectively. With this, the uncertainty of ΔT is equal to ±10 K.

In situ high-energy XRD has been carried out with the EML facility of Leibnitz IFW Dresden installed at the Swedish Materials Science Beamline P21.1 at PETRA III, DESY Hamburg. The measurements were carried out in transmission mode. The energy and the size of the monochromatic X-ray beam were 101.5 keV and 1×1 μm^2, respectively. Two-dimensional (2D) diffraction patterns were collected with the hybrid pixel detector EIGER2×4M from DECTRIS at a rate between 10 and 1000 Hz. The recording frequency of the pyrometer signal was synchronised with the X-ray detector. Powder diffraction intensities were obtained by azimuthal integration of 2D images in pyFAI [30]. An XRD pattern of LaB_6 standard powder placed in the middle of the induction coil was used to calibrate the sample-to-detector distance and detector orientation.

The solidification studies have been carried out on 35 samples of $Fe_{60}Co_{25}Ni_{10}Mo_5$ and 10 samples of $Fe_{63}Co_{26}Ni_{11}$ composition. In total 33 samples (29+4) could be preserved after the EML experiments. Weighing of the processed samples revealed an average mass loss of $\Delta m_{\mathrm{av}} = 0.01$ % in one heating-cooling cycle and $\Delta m_{\mathrm{av}} = 0.05$ % in three cycles (see Table S1 in Supplementary Material). The mass of the two samples with two processing cycles was found to increase by 0.01 %. This could be due to surface oxidation, although it is not clear at what stage this happened.

Representative samples solidified at different levels of melt undercooling were chosen for the microstructure and phase examination. They were cross-sectioned in the middle by using an electric wire discharge machine Agie Charmilles FI 440 ccS from GF Machining Solutions. One half of each sample was embedded into conductive mounting compound by using SimpliMet 3000 press from Buehler. The embedded samples were ground with SiC paper up to a grit size of P4000 and polished with diamond suspensions (particle size: 3, 1, 0.25 μm) and 0.05 μm colloidal silica. The microstructural studies were conducted by using Gemini scanning electron microscope from ZEISS equipped with EDS and EBSD detectors from Bruker. Backscattered electrons (BSE) images were taken at the acceleration voltage of 10 kV while EDS element distribution maps were recorded at 20 kV. The working distance was approx. 10 mm in both methods. EBSD patterns were collected at 20 kV accelerating voltage at 70° sample tilt angle and 18 mm working distance. The acquired EDS and EBSD data have been analysed by using the programme Esprit 2.3 from Bruker. XRD phase analysis has been carried out on ~0.5 mm thin slices cut out from the second halves of the cross-sectioned spherical samples. The slices were ground by using SiC paper with a grit size between P500 and P2400 after the electric wire discharge cutting. The XRD measurements have been carried out by using an X'Pert Pro diffractometer with Cu-K_α radiation from PANalytical. The quantitative phase analysis has been performed by using the HighScore Plus software [26].

3. Results

3.1. XRD and DSC analysis of as-cast alloys

XRD measurements of the as-cast samples (Fig. 1) only revealed the bcc phase (α-ferrite) in $Fe_{63}Co_{26}Ni_{11}$. α-Ferrite is also the major constituent of $Fe_{60}Co_{25}Ni_{10}Mo_5$ alloy. However, additional Bragg reflexes of

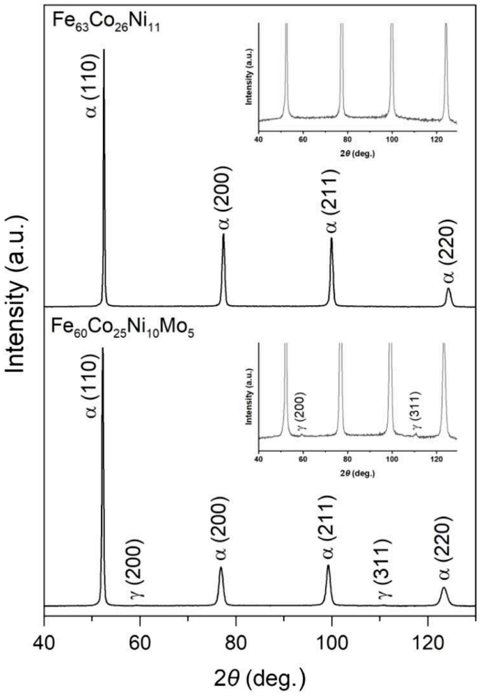

Fig. 1. XRD intensities of as-cast $Fe_{60}Co_{25}Ni_{10}Mo_5$ and $Fe_{63}Co_{26}Ni_{11}$ samples measured with Co-K_α radiation. Inserts are plotted to highlight presence of the fcc γ phase in quaternary alloy.

an fcc lattice, even if very weak, point to the presence of minor γ phase (austenite) in the sample.

DSC scans measured from $Fe_{60}Co_{40}$, $Fe_{63}Co_{26}Ni_{11}$ and $Fe_{60}Co_{25}Ni_{10}Mo_5$ samples are shown in Fig. 2. The temperatures of the identified thermal events are listed in Table 1.

The binary $Fe_{60}Co_{40}$ alloy exhibits two thermal events in the solid state. According to the Fe-Co phase diagram [31], the weak peak appearing at about 975 K is associated with the order-disorder transformation. The second peak with an onset temperature of $T_{ons} = 1255$ K is related to the magnetic as well as structural (α→γ) transformations which coincide. Although the solid-liquid transformation could not be fully accessed, the peak on melting, which corresponds to the liquidus temperature as shown by Boettinger et al. [32], has been reached. It has to be noted that the peak temperature depends on the heating rate Φ and the apparent liquidus temperature is higher than the equilibrium value [32,33]. For example, it has been shown [33] that the melting peak measured on low alloy steels shifted by up to 10 K when Φ increased from 1 to 20 K·min^{-1}. The liquidus temperature of the $Fe_{60}Co_{40}$ alloy (1770 K) obtained at $\Phi = 20$ K·min^{-1} in present work is in a good agreement with earlier publications [31,34], although lying 9–13 K above.

Similarly, the measured liquidus temperature of the $Fe_{63}Co_{26}Ni_{11}$ alloy (1761 K) conforms to the experimental data and thermodynamic calculations for the Fe-Co-Ni system [35,36]. It is 16 K higher than the predicted value, obtained by digitising Fig. 24 from Ref. [36].

Adding 5 at.% Mo to the ternary alloy results in a further decrease of the liquidus temperature of $Fe_{60}Co_{25}Ni_{10}Mo_5$ alloy to 1734 K. This relatively small decrease of T_l correlates with the effect of Mo in Fe-Mo [37], Co-Mo [38] and Ni-Mo [39] solid solutions.

The DSC data measured for $Fe_{63}Co_{26}Ni_{11}$ and $Fe_{60}Co_{25}Ni_{10}Mo_5$ samples in the solid state show essential differences compared to the binary composition. Firstly, no thermal signal could be detected which would correspond to the structural ordering in the lower temperature range for the multicomponent alloys. Secondly, two endothermic events appeared on the heating curves of $Fe_{60}Co_{25}Ni_{10}Mo_5$ and $Fe_{63}Co_{26}Ni_{11}$ alloys between approx. 1000 and 1200 K, in contrast to the just mentioned single peak of $Fe_{60}Co_{40}$ alloy. Although, only one exothermic peak is observed on the cooling curves.

3.2. High-speed video observation of crystal nucleation and growth

Selected digital images visualising solidification of $Fe_{60}Co_{25}Ni_{10}Mo_5$ and $Fe_{63}Co_{26}Ni_{11}$ samples at different levels of melt undercooling are presented in Fig. 3 and Fig. 4, respectively. Due to a higher temperature of rapidly growing solid it appears bright on a dark background of undercooled liquid or primary crystalline phase and can be distinguished clearly. Representative video clips created from full image sequences can be found in the Supplementary Material.

For the $Fe_{60}Co_{25}Ni_{10}Mo_5$ sample solidifying at low undercooling ($\Delta T = 34$ K) only one crystallization event was identified on the HSC record as shown in Fig. 3a and Video 1. The small bright particles dispersed over the sample surface are assumed to be oxides. They likely had no effect neither on nucleation nor propagation of the solid phase. In all other experiments with $Fe_{60}Co_{25}Ni_{10}Mo_5$, covering the range of melt undercooling between 97 and 306 K, the formation of two crystalline phases which appeared shortly after each other (delay time $\tau < 1$ ms) was observed (e.g. panels (b) – (e) in Fig. 3 and Video 2). The secondary phase always nucleated at multiple sites within the pre-existing crystalline phase. It quickly overtook the primary solidification front at ΔT up to about 130 K and grew behind it at higher undercoolings. According to the *in situ* XRD measurements, described in the next section, the metastable δ-ferrite was competing with the stable γ-austenite. For convenience, this phase designation is used in Fig. 3 and in following.

Nucleation and growth competition between δ-ferrite and γ-austenite was also observed for $Fe_{63}Co_{26}Ni_{11}$ samples. In contrast to $Fe_{60}Co_{25}Ni_{10}Mo_5$, experiments with the ternary alloy revealed γ appearing as a primary phase, not only at small but also at large undercoolings. For example, $Fe_{63}Co_{26}Ni_{11}$ solidified by the formation of a single γ phase at $\Delta T = 106$ K (Fig. 4a, Video 3) and 257 K (Fig. 4c) and with two crystalline phases at $\Delta T = 208$ K (Fig. 4b, Video 4) and 294 K (Fig. 4d). This is similar to the results of Kreischer [16] who observed the nucleation of single γ phase in deeply undercooled $Fe_{60}Co_{40}$ melt too. The distribution of primary nucleation events for δ and γ in dependence on the temperature of the undercooled melt for $Fe_{60}Co_{25}Ni_{10}Mo_5$ and $Fe_{63}Co_{26}Ni_{11}$ from this work and $Fe_{60}Co_{40}$ from Ref. [16] is shown in Fig. 5. For consistence, datapoints from Ref. [16] are plotted in respect to the liquidus temperature of $Fe_{60}Co_{40}$ alloy measured in the present work.

The two exothermic events associated with the release of latent heat during solidification could not be distinguished on the pyrometer curves (Fig. 6a and c) as the sampling rate was too low. In order to obtain high-resolution $T(t)$ data, the temperature was extracted from the HSC records of given crystallisation events. Conversion was done based on the relationship (Eq. (2)) between grey level H of a pixel and temperature T of a corresponding point on the sample surface [40]

$$H = A \cdot e^{-\frac{a}{T}}, \tag{2}$$

where A and a are constants. Thereby, the nucleation temperature T_n and maximum recalescence temperature measured by the pyrometer were taken as reference points. High-resolution $T(t)$ data are plotted in Fig. 6b and d for $Fe_{60}Co_{25}Ni_{10}Mo_5$ and $Fe_{63}Co_{26}Ni_{11}$, respectively.

The dendrite growth velocity v was obtained from high-speed video data under the assumption that the recorded thermal front represents the propagating solidification front. If the solid phase grew into an undercooled liquid, e.g. as γ in Fig. 3a and b or δ in Fig. 3c and d, v was calculated from the distance ΔS travelled by the thermal front in a time interval Δt. The latter was calculated from the HSC frequency and considered number of video frames. The growth velocity of the γ phase in the mushy-zone was evaluated from the change in size of individual crystallites. The estimated average uncertainty of the growth velocity was 13 % for the first method and 21 % for the second method as

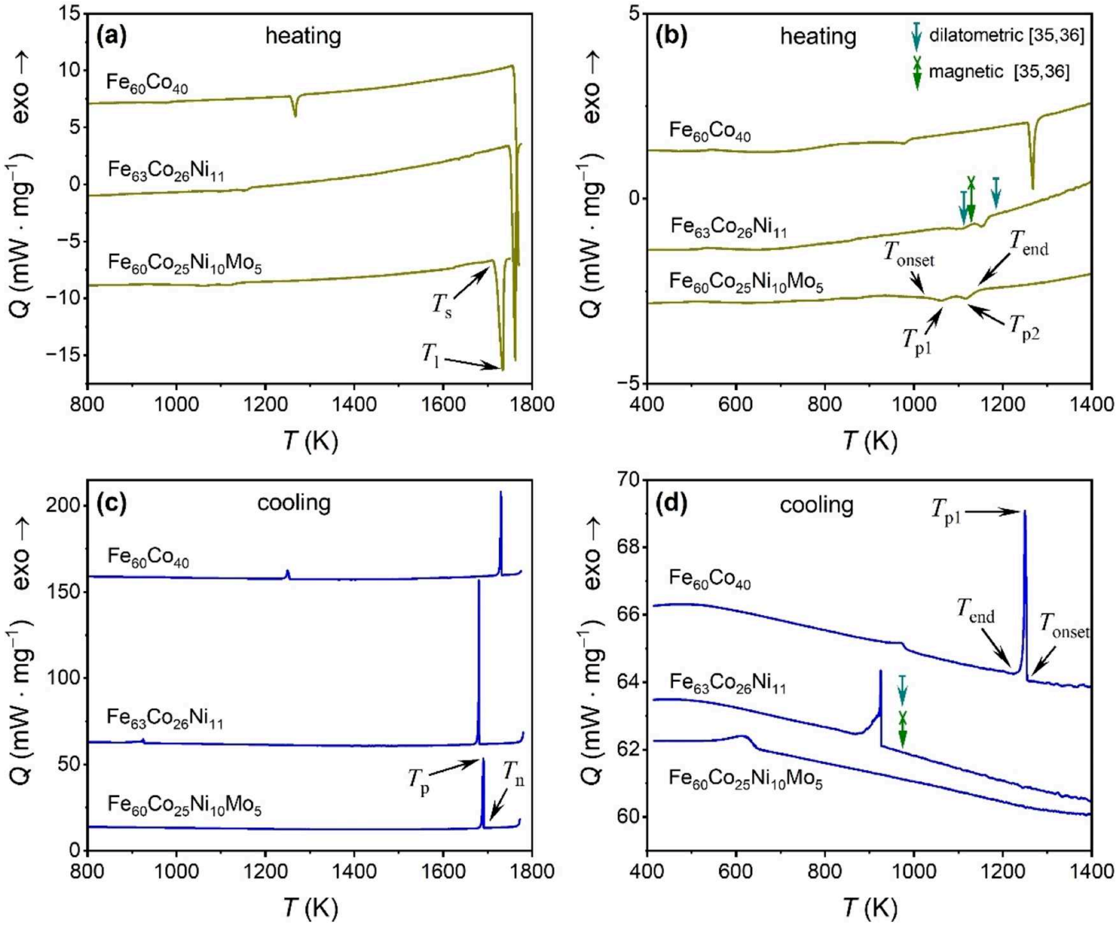

Fig. 2. DSC scans for as-cast $Fe_{60}Co_{25}Ni_{10}Mo_5$, $Fe_{63}Co_{26}Ni_{11}$ and $Fe_{60}Co_{40}$ alloys measured during heating (a,b) and cooling (c,d) at a rate of 20 K·min^{-1}. The curves are shifted on vertical axis for clarity. T_{onset}, T_{p} and T_{end} denote the onset, peak and end temperature for a given thermal event. T_{s} and T_{l} are solidus and liquidus temperatures. *Vertical arrows* at the heating and cooling curves for $Fe_{63}Co_{26}Ni_{11}$ indicate transformation temperatures for the alloy $Fe_{61.3}Co_{29}Ni_{9.7}$ ($Fe_{60}Co_{30}Ni_{10}$ in wt.%) measured by Kasé [35] (the data obtained by digitising Fig. 13 from Ref. [36]).

Table 1
Characteristic temperatures (in Kelvin) of phase transformations for $Fe_{60}Co_{25}Ni_{10}Mo_5$ and $Fe_{63}Co_{26}Ni_{11}$ alloys determined by DSC (Fig. 2). T_{ons}, T_{p} and T_{end} – onset, peak and end temperature of a thermal event; T_{s} and T_{l} – solidus and liquidus temperature.

Alloy	Heating					
	Solid-state transformation				Melting	
	T_{ons}	T_{p1}	T_{p2}	T_{end}	T_{s}	T_{l}
$Fe_{60}Co_{25}Ni_{10}Mo_5$	1038	1062	1117	1151	1711	1734
$Fe_{63}Co_{26}Ni_{11}$	1084	1109	1156	1173	1746	1761
$Fe_{60}Co_{40}$	1255	1268		1293	1755	1770
Alloy	**Cooling**					
	Solid-state transformation				**Solidification**	
	T_{ons}	T_{p1}	T_{end}		T_{n}	T_{p}
$Fe_{60}Co_{25}Ni_{10}Mo_5$	650	620	549		1693	1690
$Fe_{63}Co_{26}Ni_{11}$	927	922	864		1684	1681
$Fe_{60}Co_{40}$	1255	1250	1236		1731	1730

described in Ref. [41].

The delay time τ between nucleation of δ and γ was determined by visual inspection of HSC records. Thereby, only videos showing nucleation of both phases could be used for analysis. The uncertainty of the delay time ranged between 20 % at low undercooling ($\Delta T = 97$ K, $\tau = 0.5 \pm 0.1$ ms) and 207 % at the highest undercooling ($\Delta T = 306$ K, $\tau = 0.03 \pm 0.062$ ms). The delay time for the ternary alloy $Fe_{63}Co_{26}Ni_{11}$ could not be evaluated since the primary δ phase nucleated on the back side of the samples in all experiments carried out.

The calculated values of growth velocity v of δ and γ phases and delay time τ for the δ→γ transformation are plotted as functions of melt undercooling in Fig. 7. Also shown are the corresponding data for the binary $Fe_{60}Co_{40}$ alloy measured by using EML technique in works [14–16] for comparison.

3.3. Time-resolved synchrotron XRD measurements

Fig. 8a presents a 2D contour plot of the XRD intensities taken at 1000 Hz detector frequency and a corresponding time-temperature profile for a $Fe_{60}Co_{25}Ni_{10}Mo_5$ sample during heating and cooling in the EML facility. The full line in the lower panel shows the corrected $T(t)$ data, acquired by the pyrometer starting from 625 K. The dashed line between room temperature and 625 K is a linear interpolation. Since the measurement ended at 1190 K, an additional experiment has been carried out with the same sample in order to capture the γ→α transformation upon cooling. In this case, the X-ray detector frequency was reduced to 10 Hz and the sample was processed without melting. The contour plot elucidating the solid-state transformation during cooling is added to Fig. 8a. The dashed part of $T(t)$ line below 621 K is a linear projection to room temperature.

In agreement with the phase analysis of the as-cast $Fe_{60}Co_{25}Ni_{10}Mo_5$ sample (Fig. 1), strong reflexes of the main α phase (bcc) and weak reflexes of the minor γ phase (fcc) are present on the high-energy XRD intensities of the as-prepared sample (Fig. 8a). Only the positions of the peaks shift to smaller 2θ values due to thermal expansion as temperature

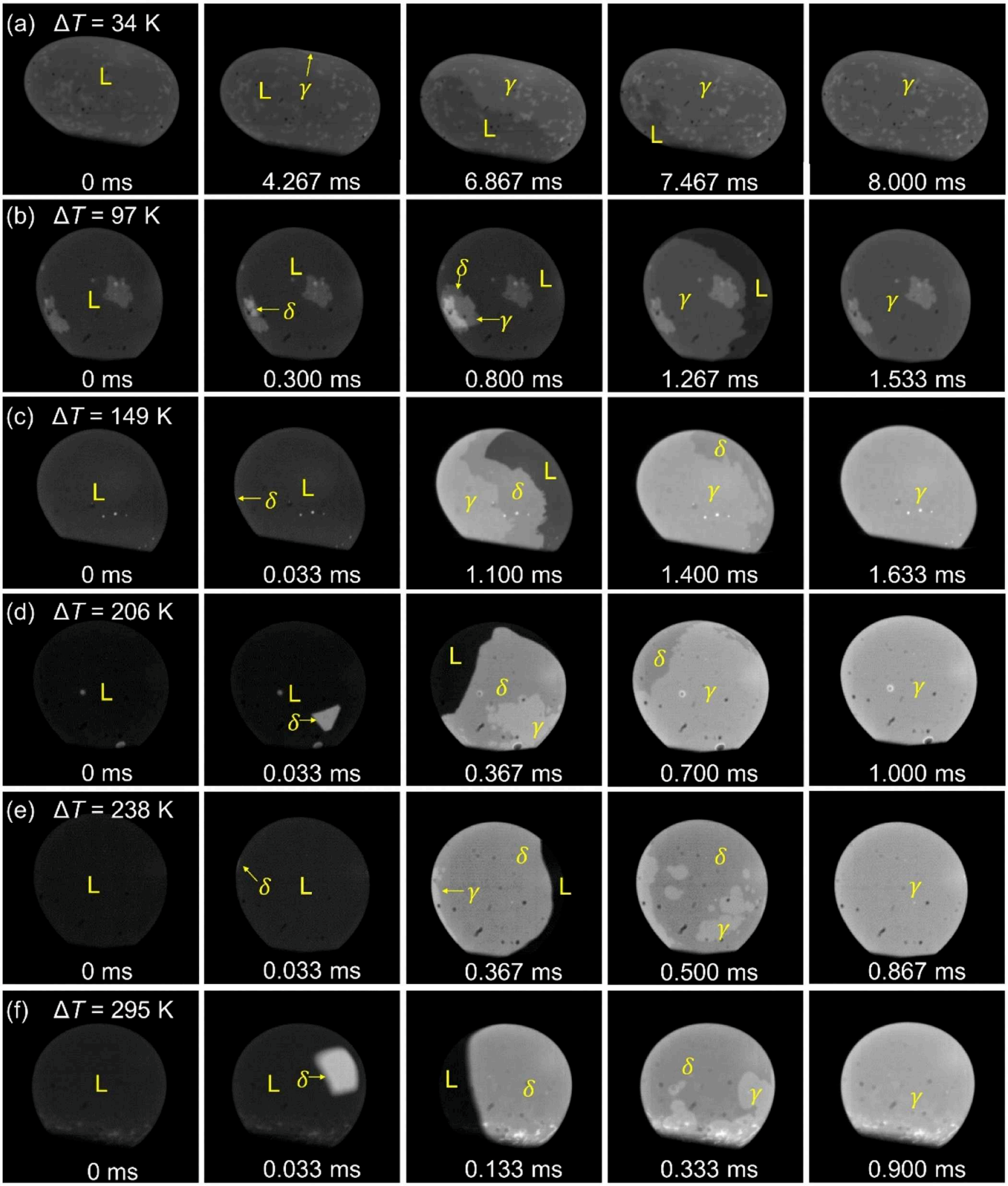

Fig. 3. Digital images showing solidification of $Fe_{60}Co_{25}Ni_{10}Mo_5$ at different undercoolings ΔT. For convenience, time is set to zero for the images of undercooled liquid shortly before crystallisation.

continuously increases. When the sample temperature reaches 1052 K it jumps to 1118 K and remains nearly constant for some time. The steep temperature rise is associated with the transformation from α ferrite to γ austenite as highlighted by a vertical dashed line in Fig. 8a. It has to be mentioned that virtually simultaneously with the onset of structural transformation, the magnetic properties of the sample change too. Further, the sample which had to be kept on a ceramic support during the initial heating began to levitate inside the induction coil.

The high-temperature fcc γ phase remains stable until melting, which sets in at $t \approx 37$ s. With this, the intensity of Bragg peaks begins to

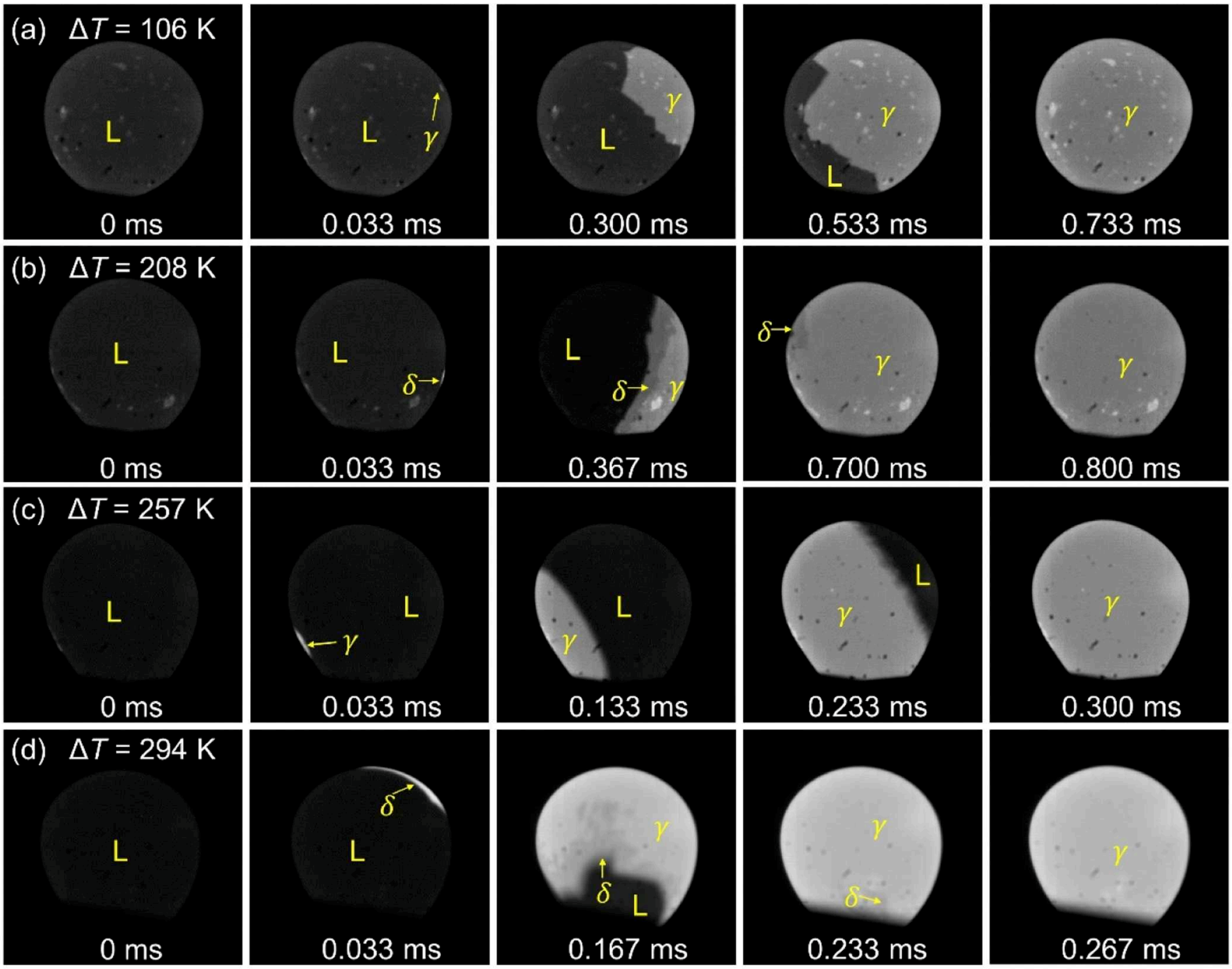

Fig. 4. Digital images showing solidification of $Fe_{63}Co_{26}Ni_{11}$ at different undercoolings ΔT. For convenience, time is set to zero for the images of undercooled liquid shortly before crystallisation.

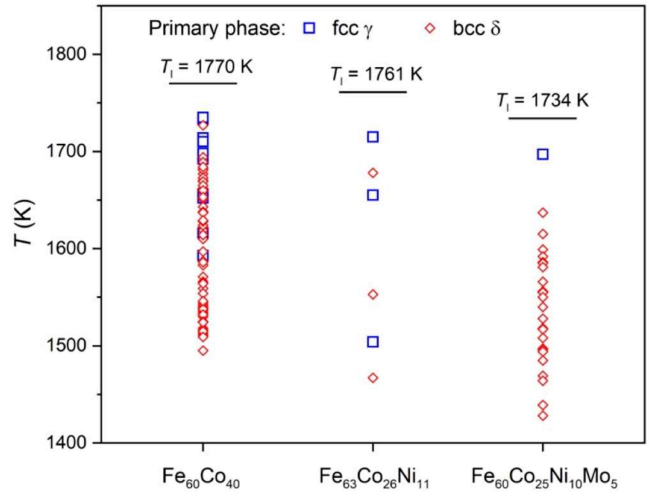

Fig. 5. Nucleation statistics for δ and γ phases emerging as a primary crystalline phase in $Fe_{60}Co_{40}$ [16], $Fe_{63}Co_{26}Ni_{11}$ and $Fe_{60}Co_{25}Ni_{10}Mo_5$ undercooled melts.

decrease and diffuse scattering from the liquid phase appears around crystalline reflexes (Fig. 8a). The temperature remains nearly constant during melting and increases quickly again when it is completed at $t \approx 47.5$ s. This point on the $T(t)$ curve is considered as the liquidus temperature $T_{\mathrm{l}}^{\mathrm{pyro}}$ and is used for the temperature correction according to Eq. (1).

XRD intensities with broad diffuse peaks have been measured for the liquid sample during heating up to 1878 K and subsequent cooling into the supercooled state. A single XRD pattern showing the liquid structure right before crystallisation is plotted in Fig. 8b, $t = 59.466$ s.

Crystallisation is indicated by strong reflexes of the fcc γ phase appearing along with a weak diffuse scattering from the melt (Fig. 8a). However, a closer look at the individual XRD profiles (Fig. 8b) reveals the coexistence of the three phases – liquid, bcc δ and fcc γ – at the very beginning of solidification ($t = 59.467$ s). The lifetime of metastable δ is less than 1 ms. Therefore, only reflexes of the γ phase can be identified on the next XRD pattern ($t = 59.468$ s). The solidification ends within a short time interval at $t \approx 60.324$ s. The growth of δ and γ phases in this $Fe_{60}Co_{25}Ni_{10}Mo_5$ sample can be seen in Fig. 3e and Video 5.

The reverse γ→α transformation started at $T = 645$ K as can be seen on the XRD and $T(t)$ data measured during cooling of the $Fe_{60}Co_{25}Ni_{10}Mo_5$ sample in another processing cycle. It sets in at significantly lower temperature, compared to α→γ on heating, and keeps going until room temperature. Furthermore, a minor fraction of the γ phase was

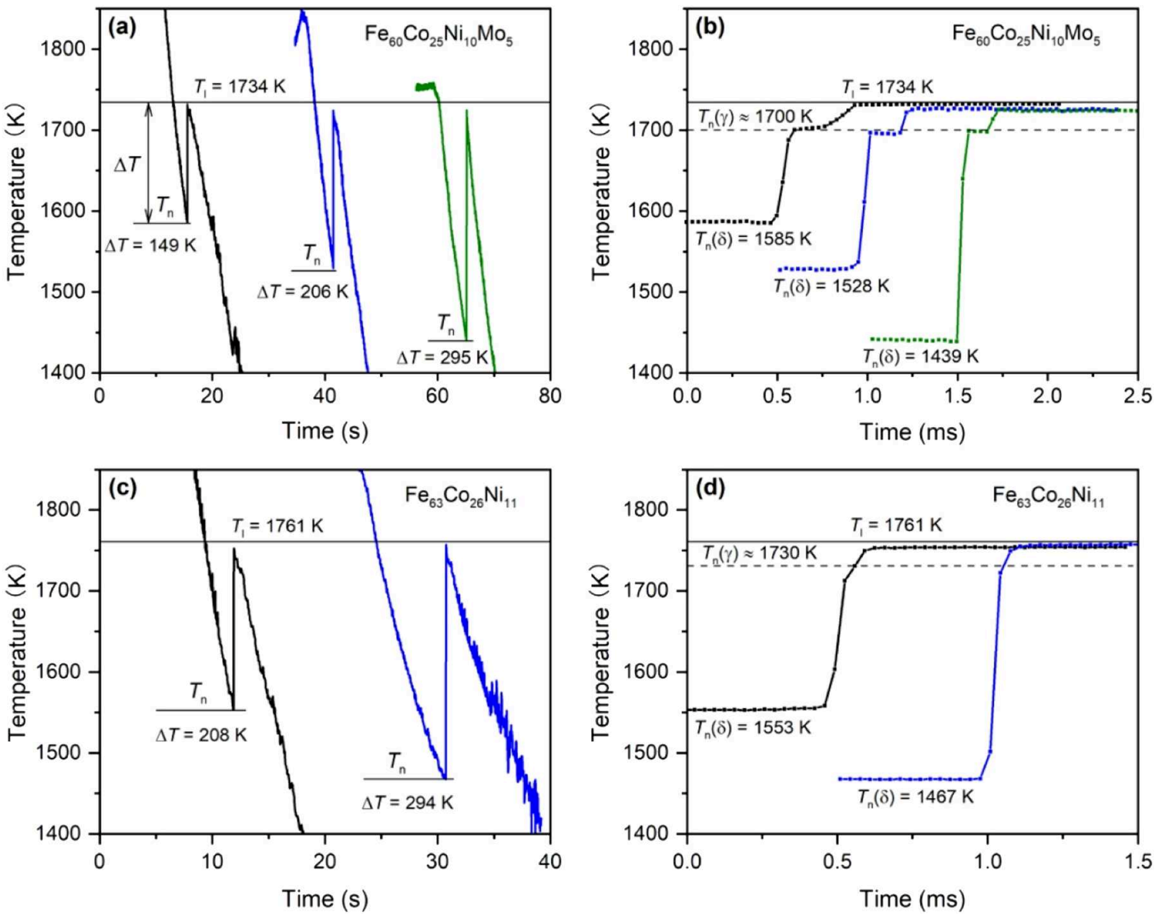

Fig. 6. Time-temperature curves for $Fe_{60}Co_{25}Ni_{10}Mo_5$ and $Fe_{63}Co_{26}Ni_{11}$ samples at the solidification stage: (a,c) measured by pyrometer; (b,d) extracted from digital images taken by high-speed camera. The curves are shifted on the time axis for clarity. T_l – liquidus temperature measured by DSC. ΔT – melt undercooling. $T_n(\delta)$ – nucleation temperature of the δ phase. $T_n(\gamma)$ – nucleation temperature of the γ phase.

found to remain untransformed.

Only formation of the γ phase could be caught for $Fe_{63}Co_{26}Ni_{11}$ samples. This might be due to a limited number of the experiments, a lower probability for nucleation of δ-ferrite or short delay time between nucleation of δ and γ in this alloy. Contour plot of the XRD intensities measured from the $Fe_{63}Co_{26}Ni_{11}$ sample in a whole heating-cooling cycle is shown in Fig. 9. The high-temperature range of $T(t)$ curve between approx. 1280 and 2060 K, drawn in grey, was impacted by oxides appearing on the sample's surface.

The α→γ transformation occurred upon heating between 1047 and 1120 K, which is nearly the same as in the alloy with Mo. However, it went notably faster as indicated by a short thermal arrest on the $T(t)$ curve. Magnetic properties of $Fe_{63}Co_{26}Ni_{11}$ samples were observed to change simultaneously with the structural transformation. The reverse γ→α transformation in the $Fe_{63}Co_{26}Ni_{11}$ alloy began at a notably higher temperature (946 K vs. 645 K) and ended at 678 K.

3.4. Microstructure and phase analysis after EML processing

The SEM backscattered electrons images taken from cross-sections of the EML processed $Fe_{60}Co_{25}Ni_{10}Mo_5$ and $Fe_{63}Co_{26}Ni_{11}$ samples are presented in Fig. 10. Despite the similarities in growth kinetics of crystalline phases in both alloys, the resulting microstructures are strikingly different. $Fe_{60}Co_{25}Ni_{10}Mo_5$ alloy (Fig. 10a) exhibits dendritic pattern with pronounced microsegregation of Mo at ΔT up 249 K at least. At the highest achieved undercooling of 330 K the grain morphology changes to a lath-like one. Since Fe, Co and Ni are neighbors in the periodic system, the BSE micrographs of the $Fe_{63}Co_{26}Ni_{11}$ samples are rather blurred (Fig. 10b). The apparent contrast on the images could be related to the electron channeling effects in dendrites or dendrite branches with different orientation.

More comprehensive information on the microstructure of the solidified samples has been obtained by using EDS and EBSD analysis. The element distribution maps (Figs. 11, 12) show that $Fe_{60}Co_{25}Ni_{10}Mo_5$ and $Fe_{63}Co_{26}Ni_{11}$ alloys are characterized by micro-segregation of solute atoms at the melt undercooling up to approx. 250 K. However, the composition of dendritic and interdendritic regions is essentially different. In $Fe_{60}Co_{25}Ni_{10}Mo_5$ samples, dendrites are enriched with Fe and Co, whereas interdendritic regions are enriched with Mo. Ni atoms are rather homogeneously dispersed over the scanned areas. In $Fe_{63}Co_{26}Ni_{11}$ samples, it is Ni that segregates into interdendritic regions, while dendrites are enriched with Fe and Co similarly to the quaternary alloy. Microsegregation is found to be essentially reduced for both alloys if melt undercooling increases to 295 K.

Microstructure analysis also revealed the presence of minor hole-like structures on the examined $Fe_{60}Co_{25}Ni_{10}Mo_5$ cross-sections. The locations of these holes on the SEM micrographs correspond to the Mo-enriched spots on the EDS maps (Fig. 11). This is particularly well seen on the SEM images taken with larger magnification (Fig. S1 in Supplementary Material). Presumably, the holes were formed under mechanical impact during metallographic preparation by pulling out Mo-rich inclusions. This assumption is supported by finding Mo-eniched particles with similar morphology on untreated surfaces of the samples solidified at large undercooling as shown in Fig. S2 in the Supplementary Material ($\Delta T = 249$ K, $\Delta T = 295$ K and $\Delta T = 330$ K).

The EBSD analysis showed that grain morphology and size greatly

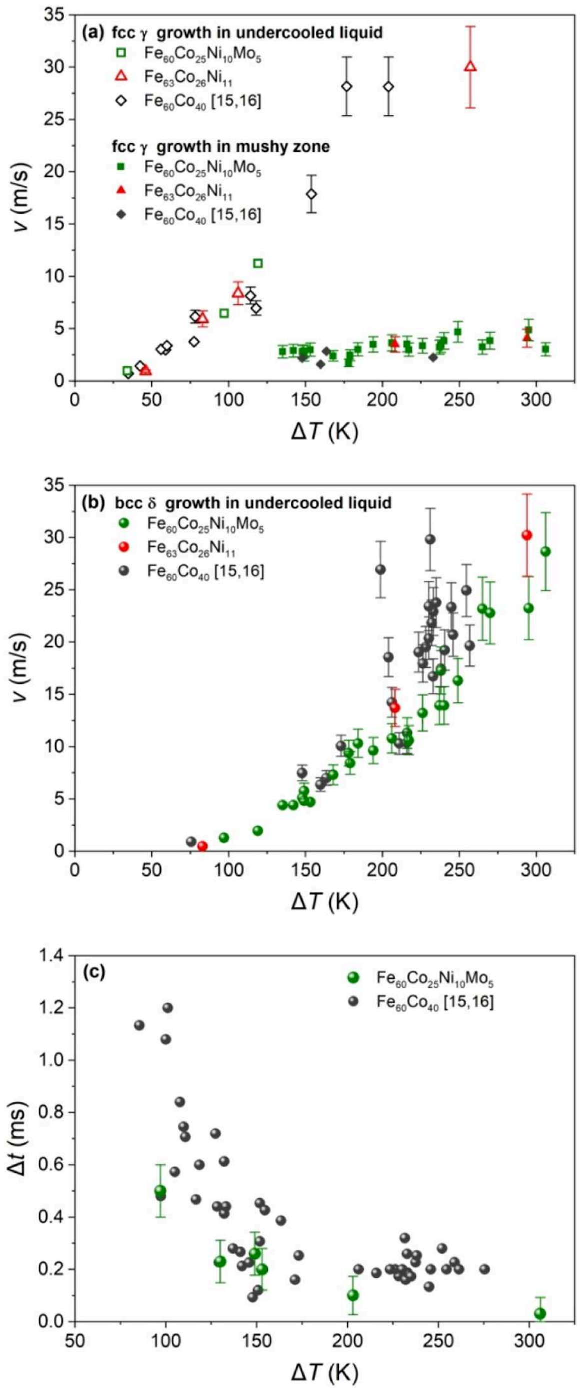

Fig. 7. Nucleation and growth competition of δ and γ phases during solidification of $Fe_{60}Co_{25}Ni_{10}Mo_5$, $Fe_{63}Co_{26}Ni_{11}$ and $Fe_{60}Co_{40}$ [15,16] undercooled melts: (a) growth velocity of the δ phase; (b) growth velocity of the γ phase; (c) delay time τ for the δ→γ transformation in $Fe_{60}Co_{25}Ni_{10}Mo_5$. The uncertainty bars for the growth velocity data are only shown if they are larger than the size of symbol.

differ for both compositions (Fig. 13). $Fe_{63}Co_{26}Ni_{11}$ samples are predominated by coarse, equiaxed, several hundreds of microns large grains. It appears that the melt undercooling has no significant effect on the microstructure of this alloy. In $Fe_{60}Co_{25}Ni_{10}Mo_5$ samples, the grain size in general is significantly smaller and grain morphology is largely dependent on undercooling. In the lower undercooling range up to $\Delta T =$ 148 K, microstructure is characterised by equiaxed grains with a mean size of about 15 μm. When undercooling increases up to 184 K and further to 295 K, grains become columnar, extending more than 150 μm in length. At the largest achieved undercooling, $\Delta T = 330$ K, grains change again, getting a lath-shaped morphology typical for martensite.

Room temperature XRD intensities for the $Fe_{60}Co_{25}Ni_{10}Mo_5$ samples solidified at different undercoolings and the results of Rietveld refinement are presented in Fig. S3 and Table S2 in the Supplementary Material. In agreement with the phase analysis of the as-cast alloy and *in situ* high-energy XRD measurements, Bragg peaks of the main α phase (bcc) and minor γ phase (fcc) could be clearly identified. The intensity of the diffraction peaks of the γ phase shows a very small change for samples solidified at ΔT up to 184 K, decreases to virtually zero at ΔT of 249 K and 295 K and notably increases at the largest undercooling of 330 K (Fig. S3a). The volume fraction of γ obtained by Rietveld refinement exhibits a similar dependence on melt undercooling, decreasing from ∼9 % at $\Delta T = 34$ K to ∼2 % at $\Delta T = 295$ K and increasing to ∼19 % at $\Delta T =$ 330 K (Fig. S3b, Table S2).

4. Discussion

4.1. Nucleation competition between metastable δ and stable γ phase

The distribution of nucleation temperatures T_n for bcc (δ) and fcc (γ) as a primary phase (Fig. 5) revealed that alloying $Fe_{60}Co_{40}$ with Ni and Mo has a significant but different impact on phase competition.

Kreischer [16] analysed the temperature dependence of the activation energy $\Delta G^* \sim \left(\sigma^3/\Delta G_V^2\right)\cdot f_{cat}$ (σ – solid-liquid interfacial energy; ΔG_V – Gibbs free energy difference per volume; f_{cat} – catalytic factor for heterogeneous nucleation) for the nucleation of δ and γ in $Fe_{60}Co_{40}$. Since the Gibbs free energy difference ΔG_V is larger for stable γ, the preferred nucleation of metastable δ suggests a lower interfacial energy for a bcc structured crystal compared to fcc as predicted by models [42–44]. Assuming heterogeneous nucleation with the same catalytic factor f_{cat} for both phases it was found that the formation of metastable δ is favourable at melt undercoolings larger than 76 K. The solidification experiments [16] have shown, however, that any phase (either δ or γ) can nucleate in a wide range of ΔT between 43 and 177 K (Fig. 5). The observation that there is no sharp transition with rising undercooling at a critical value can be understood as a distribution of inoculants (e.g. oxides) with a spectrum of f_{cat}-values as discussed by Kelly and Vander Sande [45]. The distribution of heterogeneous nucleation sites may depend on melt purity and processing conditions such as maximum temperature or thermal hold. As the catalytic factor f_{cat} can be different for fcc and bcc, nucleation of the stable or metastable phase can be promoted within a transition range of ΔT.

Substitution of Co with fcc Ni in the ternary alloy apparently extends the range of undercooling where nucleation of both phases is possible. In contrast to that, alloying $Fe_{63}Co_{26}Ni_{11}$ with 5 at.% Mo clearly favours nucleation of metastable δ in undercooled $Fe_{60}Co_{25}Ni_{10}Mo_5$ melts. Starting at $\Delta T = 97$ K, all quaternary samples solidified through formation of the primary δ phase. This might have two explanations: i) Mo-rich particles found in the microstructure of solidified samples (Fig. 11) provide heterogeneous nucleation sites for δ, and ii) adding Mo with the bcc crystal structure decreases the activation energy for nucleation of the bcc δ phase.

The assumption on heterogeneous nucleation in $Fe_{60}Co_{25}Ni_{10}Mo_5$ is supported by a fine-grained microstructure of processed samples (Fig. 13). Although not detected by high-temperature XRD, it is likely that Mo-enriched particles precipitate in the undercooled melt and act as inoculants for δ as well as for γ phase. Indeed, fine-grained microstructure has been formed in the samples solidified with primary γ (Fig. 13a, $\Delta T = 34$ K) and primary δ phase (Fig. 13a, $\Delta T = 149$ K). The preferred nucleation of metastable δ at $\Delta T \geq 97$ K might be associated with additional reduction of the nucleation barrier as discussed above.

High-speed photography records (Figs. 3, 4 and video clips in Supplementary Material) showed that growth of γ as the secondary phase

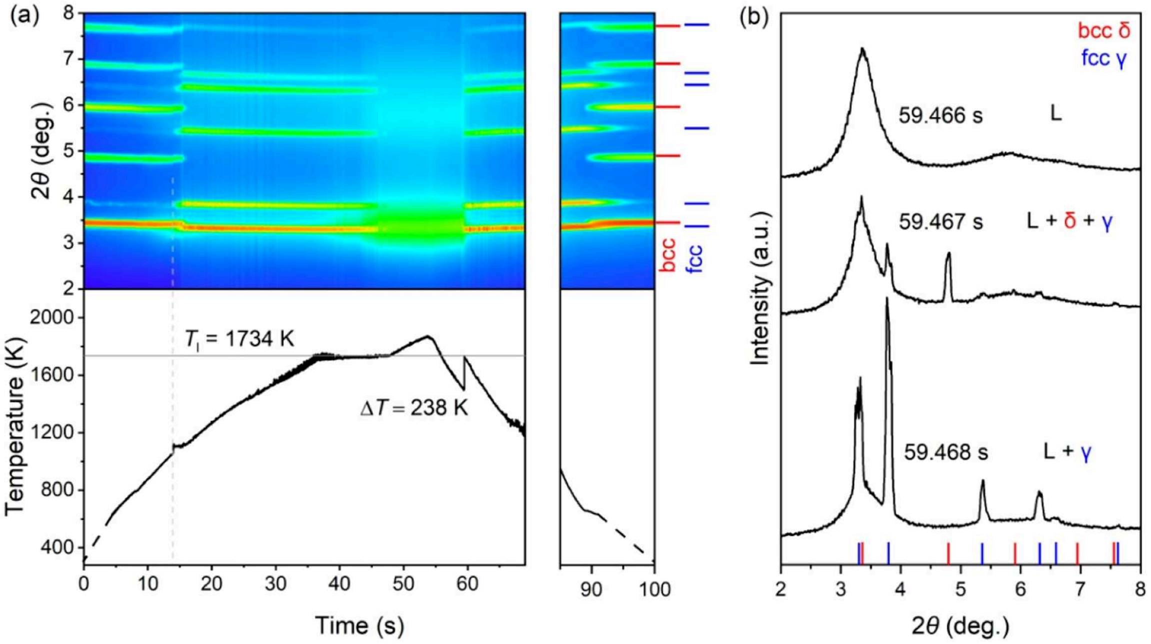

Fig. 8. (a) Compilation of XRD contour plots and time-temperature profiles for $Fe_{60}Co_{25}Ni_{10}Mo_5$ samples processed in EML facility. *Dashed* parts of the $T(t)$ lines are linear interpolations between room temperature and a lowest point measured by pyrometer. *Vertical dashed line* at t = 13.92 s denotes onset of the α→γ transformation during heating. (b) Subsequently recorded XRD patterns showing (i) undercooled liquid L at t = 59.466 s; (ii) coexistence of the L, δ and γ phases at t = 59.467 s; (iii) coexistence of the L and γ phases at t = 59.468 s.

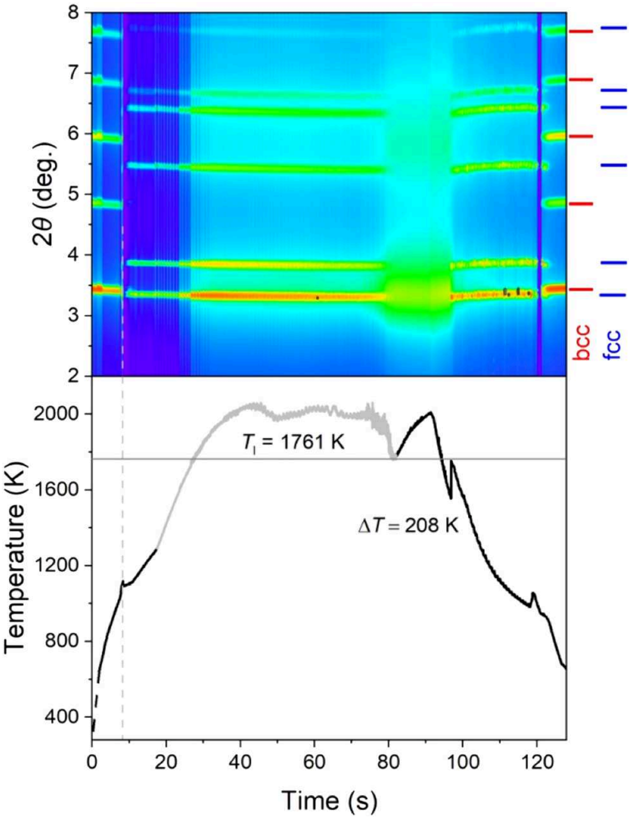

Fig. 9. XRD contour plot and time-temperature profile for $Fe_{63}Co_{26}Ni_{11}$ sample solidified at ΔT = 208 K. $T(t)$ curve in *light grey* corresponds to the pyrometer readings impacted by oxides on sample surface. *Vertical dashed line* at t = 8.26 s denotes onset of the α→γ transformation during heating.

always started within the primary δ. This behaviour conforms to the earlier reports on double recalescence in Fe-rich alloys [14–16,22–24] as well as in CrFeNi, CoCrNi and CoCrFeNi medium- and high-entropy alloys [25].

Koseki and Flemings [20] analysed possible configurations for the nucleation of γ phase at presence of the solid δ and undercooled liquid in Fe-Cr-Ni alloys. It was concluded that the fcc phase most likely nucleates at the bcc/bcc grain boundaries. The observation of the correlation between the dependences of delay time τ on melt undercooling (similar to that in Fig. 7c) as well as on the fraction solid of primary bcc was supposed to support that. The delay time for nucleation of fcc was suggested to steeply decrease when bcc/bcc boundaries form in a sufficient amount of primary bcc, occurring at ΔT between approx. 100 and 150 K in Fe-Cr-Ni.

Kreischer and Volkmann [15] also related delay time τ to the fraction of the primary δ, although under assumption of the heterogeneous nucleation of the γ phase at the interface between δ and undercooled liquid. In their approach, based on classical theory, the nucleation rate of γ was considered to be proportional to the number of possible heterogeneous nucleation sites and consequently to the area of the δ/liquid interface.

Matson [46] recently proposed the retained damage model (RDM) to explain the dependence of delay time τ on melt undercooling and convection. The main idea of RDM is that lattice defects (dislocations, tilt low angle grain boundaries) and lattice strain introduced during growth of primary δ make an additional contribution to the driving force for δ→γ transformation. The number of defects essentially depends on growth velocity and on undercooling of the melt, respectively. On the other hand, the driving force caused by the difference in free energy of δ and γ phases at $T_n(\gamma)$ does not vary. Indeed, high-resolution $T(t)$ data (Fig. 6) show that independently of nucleation temperature $T_n(\delta)$, the δ→γ transformation sets in at a constant temperature: $T_n(\gamma) = 1700 \pm 7$ K in $Fe_{60}Co_{25}Ni_{10}Mo_5$ and $T_n(\gamma) \approx 1730$ K in $Fe_{63}Co_{26}Ni_{11}$.

4.2. Dendrite growth kinetics

In general, the measured $v(\Delta T)$ dependences for δ and γ phases

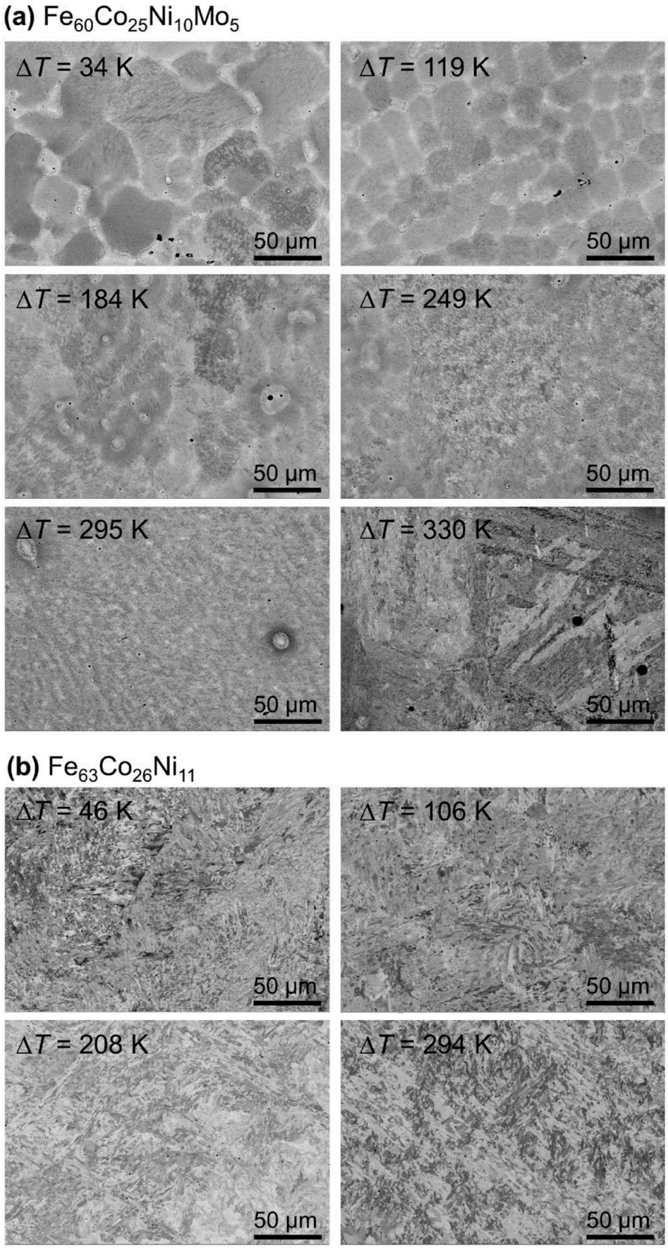

Fig. 10. SEM BSE images of cross-sectioned samples solidified at different undercooling ΔT: (a) $Fe_{60}Co_{25}Ni_{10}Mo_5$ composition; (b) $Fe_{63}Co_{26}Ni_{11}$ composition.

growing into undercooled liquid exhibit continuous growth upon increasing undercooling (Fig. 7). In the lower range of ΔT up to approx. 200 K, there is a good agreement of $v_\delta(\Delta T)$ in $Fe_{60}Co_{25}Ni_{10}Mo_5$, $Fe_{63}Co_{26}Ni_{11}$ and $Fe_{60}Co_{40}$ alloys (Fig. 7a). Similarly, $v_\gamma(\Delta T)$ of all three alloys agree at ΔT below 120 K (Fig. 7b). At higher undercoolings, $v_\delta(\Delta T)$ and $v_\gamma(\Delta T)$ in ternary and quaternary alloys appear to deviate to smaller values compared to $Fe_{60}Co_{40}$ binary. This behaviour correlates with microstructural changes occurring at similar levels of undercooling, particularly with the remarkable homogenisation observed on EDS element distribution maps in Figs. 11 and 12. Probably, the present results on dendrite growth rate can be explained by an increasing difference between temperature dependences of atomic mobility of the three molten alloys upon increasing undercooling. On the other hand, trapping of solute atoms (Ni and Mo) into growing dendrites might result in decreasing mobility at the solidification front.

In contrast to the dendrite growth in undercooled melts, the growth rate of γ during the transformation of metastable δ exhibits a very weak dependence on initial ΔT. As shown in Fig. 6, the δ→γ transformation occurs at the same temperature $T_n(\gamma)$ independently on $T_n(\delta)$. Hence, the driving force due to the free energy difference between two phases is constant. Matson and Hyers [47] proposed a growth model for stable γ into a mushy-zone consisting of primarily solidified metastable δ dendrites and remaining liquid. Rodriguez and Matson [48] have further developed the model and found a unique relation between growth velocity of γ and the undercooling $\Delta T_\gamma = T_l(\gamma) - T_n(\gamma)$. Accordingly, the growth rate of the secondary phase is independent on the bulk undercooling prior to solidification as observed in the experiments.

4.3. Phase transformations and microstructure evolution

The temperature of the solid-state transformations for the $Fe_{63}Co_{26}Ni_{11}$ alloy obtained by DSC in the present work shows a good agreement with the dilatometric measurements by Kasé [35] and Calphad calculations by Guillermet [36]. We refer to Ref. [36] which presents the data of Kasé. Considering the vertical section of the Fe-Co-Ni diagram at 10 wt.% Ni [36] the endothermic events registered upon heating of solid $Fe_{63}Co_{26}Ni_{11}$ and $Fe_{60}Co_{25}Ni_{10}Mo_5$ can be assigned to the α→γ and ferromagnetic-to-paramagnetic transformation. The exothermic signals on the cooling curves are also related to these transformations, which set in simultaneously upon reaching a certain undercooling of the solid below equilibrium. The temperatures of the structural and magnetic transformations for the ternary alloy with an approximate composition of $Fe_{61.3}Co_{29}Ni_{9.7}$ ($Fe_{60}Co_{30}Ni_{10}$ in wt.%), obtained by digitising Fig. 13 from Ref. [36], are indicated on DSC curves for $Fe_{63}Co_{26}Ni_{11}$ in Fig. 2. The decrease of the onset temperature for structural and magnetic transformations in the $Fe_{63}Co_{26}Ni_{11}$ alloy can be explained by extending the stability range for γ as well as a lower Curie-temperature of Ni [49].

Molybdenum has much stronger impact on the microstructure as well as structural and magnetic transformations in the $Fe_{60}Co_{25}Ni_{10}Mo_5$ alloy. Although interdiffusion of Mo in α-Fe and γ-Fe is higher than that of Co and Ni and higher than self-diffusion of Fe [50,51] it readily segregates to the interdendritic regions during solidification (Fig. 11). Addition of Mo significantly decreases the onset temperature of the solid-state transformation occurring on cooling and leads to appearance of retained austenite in the as-cast and EML processed $Fe_{60}Co_{25}Ni_{10}Mo_5$ samples. This phenomenon can possibly be assigned to the solute drag effect known to occur in Mo-alloyed steels [52–55]. Segregation of Mo to the γ/γ or α/γ interface essentially retards its migration, slows the transformation kinetics or even causes incomplete transformation. This provides the effective means to control austenite transformation and tailor the microstructure and performance of high-strength steels.

The change from pronounced microsegregation of Mo at $\Delta T \leq 249$ K (Fig. 11a–d) to rather a homogeneous distribution at larger undercoolings (Fig. 11e,f) can be explained by solute trapping. The subsequent cooling of the supersaturated γ phase results in formation of lath martensite (Figs. 10a and 13a, $\Delta T = 330$ K). This transformation is presumably favoured by dislocations and/or other lattice defects generated during rapid solidification. The dislocations in austenite are known to be conducive to the martensitic transformation [56,57].

5. Conclusions

In this work, the solidification of undercooled $Fe_{60}Co_{25}Ni_{10}Mo_5$ and $Fe_{63}Co_{26}Ni_{11}$ melts, phase formation and structural evolution have been studied *in situ* by using electromagnetic levitation, high-speed video and high-energy synchrotron XRD. Due to a high acquisition rate (1000 Hz) of the X-ray detector, it was possible to register the formation of the metastable primary phase with a lifetime below 1 ms. The *in situ* measurements have been complemented by microstructural analysis of solidified samples, conventional XRD, and differential scanning calorimetry. The results obtained for $Fe_{60}Co_{25}Ni_{10}Mo_5$ and $Fe_{63}Co_{26}Ni_{11}$

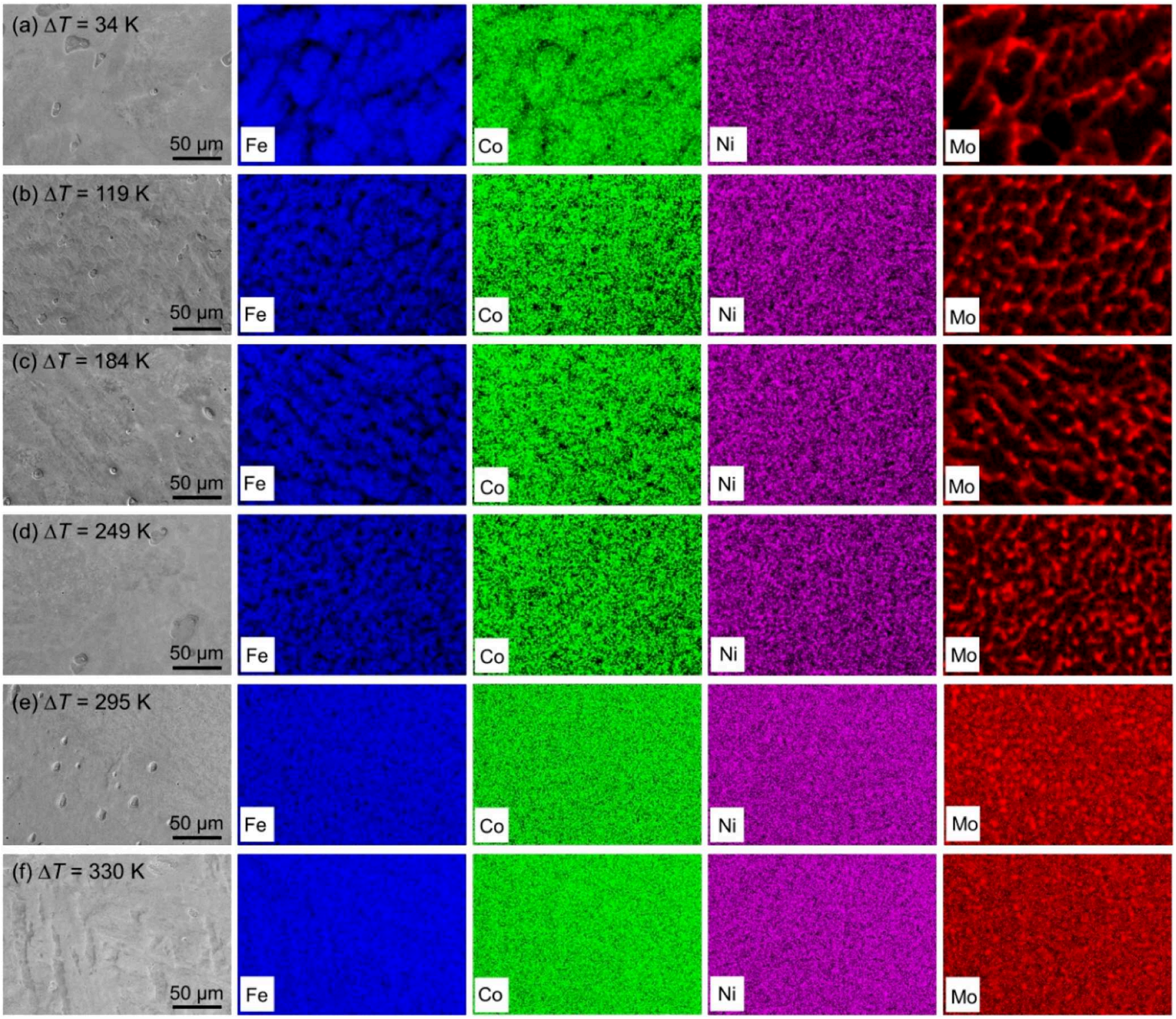

Fig. 11. SEM SE overview images and EDS element distribution maps for $Fe_{60}Co_{25}Ni_{10}Mo_5$ samples solidified at different melt undercooling: (a) $\Delta T = 34$ K; (b) $\Delta T = 119$ K; (c) $\Delta T = 184$ K; (d) $\Delta T = 249$ K; (e) $\Delta T = 295$ K; (f) $\Delta T = 330$ K.

alloys have been analysed with respect to reported data for the binary $Fe_{60}Co_{40}$ composition [15–17]. Key findings can be summarized as following.

(1) At small undercoolings, up to about 50 K, only the stable γ phase (fcc structure) grew from the melt. At higher undercoolings, solidification of the $Fe_{60}Co_{25}Ni_{10}Mo_5$ alloy always proceeded through formation of the metastable δ phase (bcc structure) which subsequently transformed to γ. In the ternary $Fe_{63}Co_{26}Ni_{11}$ as well as binary $Fe_{60}Co_{40}$ melts, both solidification pathways have been observed at large undercoolings, despite a smaller activation energy for δ. The formation of primary γ might be explained by heterogeneous nucleation.

(2) Dendrite growth of the δ and γ phases did not exhibit any obvious difference by changing from binary $Fe_{60}Co_{40}$ to ternary $Fe_{63}Co_{26}Ni_{11}$ and to quaternary $Fe_{60}Co_{25}Ni_{10}Mo_5$. The growth rate of both phases in the undercooled liquid continuously increased upon increasing ΔT, whereas growth velocity of γ in the mushy-zone was relatively small and independent on the initial melt undercooling.

(3) The delay time between nucleation of metastable δ and the transformation to stable γ showed a strong dependence on melt undercooling, quickly decreasing in the lower ΔT-range below 130 K.

(4) Ni and Mo alloying had a notable impact on the phase transformations in ternary and quaternary alloys. Compared to binary $Fe_{60}Co_{40}$, structural and magnetic transformations occur separately, at a lower temperature, and with a larger hysteresis in heating-cooling cycles.

(5) The microstructure of ternary $Fe_{63}Co_{26}Ni_{11}$ did not show any significant dependence on melt undercooling. Only a weak decrease of grain size and more homogeneous distribution of Ni atoms were observed in samples solidified at large ΔT.

(6) A fine-grained microstructure consisting of ferrite and minor fraction of retained austenite was observed in the $Fe_{60}Co_{25}Ni_{10}Mo_5$ samples for ΔT up to approx. 200 K. The grain-refining was presumably caused by heterogeneous nucleation on Mo-enriched particles precipitating in the undercooled melt. A pronounced change from small equiaxed to large columnar grains occurred in a sample solidified at $\Delta T = 295$ K. The microstructure has undergone another

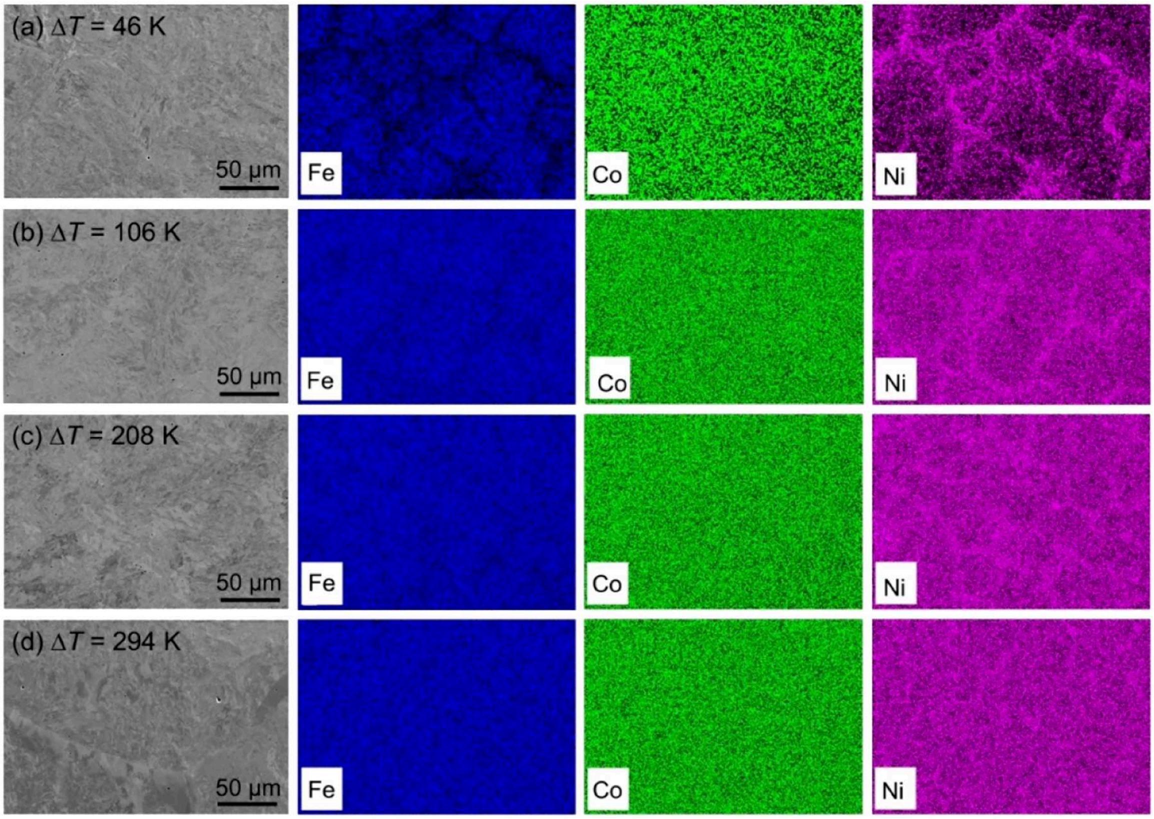

Fig. 12. SEM SE overview images and EDS element distribution maps for $Fe_{63}Co_{26}Ni_{11}$ samples solidified at different melt undercooling: (a) $\Delta T = 46$ K; (b) $\Delta T = 106$ K; (c) $\Delta T = 208$ K; (d) $\Delta T = 294$ K.

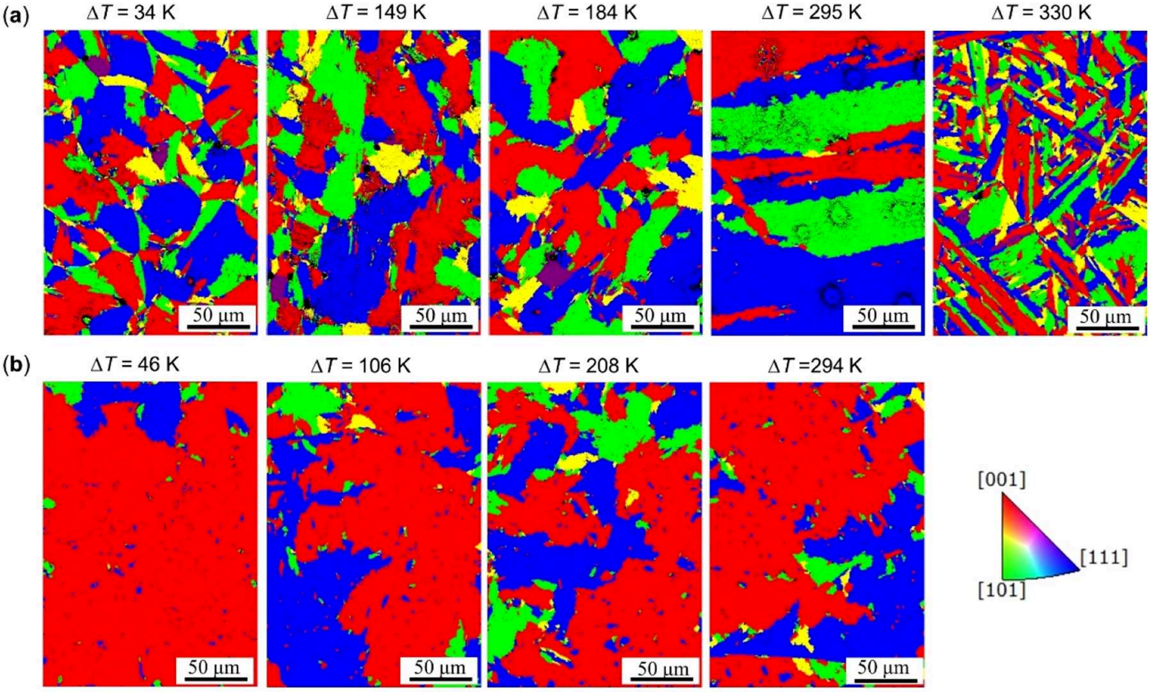

Fig. 13. Crystal orientation maps for (a) $Fe_{60}Co_{25}Ni_{10}Mo_5$ and (b) $Fe_{63}Co_{26}Ni_{11}$ samples solidified at different undercooling.

transformation in the sample solidified at $\Delta T = 330$ K where lath martensite was formed. Furthermore, addition of Mo hindered the γ→α transition, causing the appearance of retained austenite in $Fe_{60}Co_{25}Ni_{10}Mo_5$ samples.

CRediT authorship contribution statement

Shilei Liu: Writing – review & editing, Writing – original draft, Visualization, Software, Investigation, Formal analysis, Conceptualization. **Victoria Kaban:** Writing – review & editing, Investigation. **Olof Gutowski:** Software, Investigation. **Thomas Volkmann:** Writing – original draft. **Kornelius Nielsch:** Writing – review & editing, Supervision. **Ivan Kaban:** Writing – review & editing, Writing – original draft, Resources, Methodology, Investigation, Formal analysis, Data curation, Conceptualization.

Declaration of competing interest

The authors declare that they have no known competing financial interests or personal relationships that could have appeared to influence the work reported in this paper.

Acknowledgments

We acknowledge DESY (Hamburg, Germany), a member of the Helmholtz Association HGF, for the provision of experimental facilities. Parts of this research were carried out at PETRA III and we would like to thank J. Liu and P. Glaevecke for assistance in using beamline P21.1. Beamtime was allocated for proposal I-20241031. M. v. Zimmerman is acknowledged for valuable suggestions and discussions during preparation of beamtime application as well as high-energy XRD measurements. S. Liu acknowledges financial support from China Scholarship Council (CSC) for his Ph.D. study. T. Volkmann acknowledges the support from the European Space Agency ESA in the frame of the projects PARSEC and MAGNEPHAS (Grant No. 4200014980). S. Liu is indebted to B. Bartusch for the DSC measurements, B. Opitz for the help with laboratory XRD, S. Donath for the alloy melting guidance, and C. Schicker and N. Geißler for the introduction to metallographic sample preparation. T.G. Woodcock is gratefully acknowledged for the stimulating discussions and comments during preparation of the manuscript.

Supplementary materials

Supplementary material associated with this article can be found, in the online version, at doi:10.1016/j.actamat.2025.121017.

References

[1] J.W. Yeh, S.K. Chen, S.J. Lin, J.Y. Gan, T.S. Chin, T.T. Shun, C.H. Tsau, S.Y. Chang, Nanostructured high-entropy alloys with multiple principal elements: novel alloy design concepts and outcomes, Adv. Eng. Mater. 6 (2004) 299–303.

[2] B. Cantor, I.T.H. Chang, P. Knight, A.J.B. Vincent, Microstructural development in equiatomic multicomponent alloys, Mater. Sci. Eng. A 375-377 (2004) 213–218.

[3] D. Ma, M. Yao, K.G. Pradeep, C.C. Tasan, H. Springer, D. Raabe, Phase stability of non-equiatomic CoCrFeMnNi high entropy alloys, Acta Mater. 98 (2015) 288–296.

[4] K. Biswas, J.W. Yeh, P.P. Bhattacharjee, J.T.M. DeHosson, High entropy alloys: key issues under passionate debate, Scr. Mater. 188 (2020) 54–58.

[5] S.A. Kube, J. Schroers, Metastability in high entropy alloys, Scr. Mater. 186 (2020) 392–400.

[6] E.P. George, W.A. Curtin, C.C. Tasan, High entropy alloys: a focused review of mechanical properties and deformation mechanisms, Acta Mater. 188 (2020) 435–474.

[7] D.B. Miracle, O.N. Senkov, A critical review of high entropy alloys and related concepts, Acta Mater. 122 (2017) 448–511.

[8] E.P. George, D. Raabe, R.O. Ritchie, High-entropy alloys, Nat. Rev. Mater. 4 (2019) 515–534.

[9] W. Li, D. Xie, D. Li, Y. Zhang, Y. Gao, P.K. Liaw, Mechanical behavior of high-entropy alloys, Prog. Mater. Sci. 118 (2021) 100777.

[10] H. Kwon, P. Sathiyamoorthi, M.K. Gangaraju, A. Zargaran, J. Wang, Y.U. Heo, S. Harjo, W. Gong, B.J. Lee, H.S. Kim, High-density nanoprecipitates and phase reversion via maraging enable ultrastrong yet strain-hardenable medium-entropy alloy, Acta Mater. 248 (2023) 118810.

[11] R. Hermann, W. Löser, G. Lindenkreuz, A. Diefenbach, W. Zahnow, W. Dreier, T. Volkmann, D. Herlach, Metastable phase formation in undercooled Fe–Co melts, Mater. Sci. Eng. A 375-377 (2004) 507–511.

[12] R. Hermann, W. Löser, Growth kinetics of undercooled Fe–Co melts, J. Magn. Magn. Mater. 242–245 (2002) 285–287.

[13] N. Liu, F. Liu, G.C. Yang, Y.Z. Chen, C.L. Yang, Y.H. Zhou, Nucleation and phase selection in undercooled Fe–Co melt, J. Alloy. Compd. 467 (2009) L11–L15.

[14] J.E. Rodriguez, C. Kreischer, T. Volkmann, D.M. Matson, Solidification velocity of undercooled Fe–Co alloys, Acta Mater. 122 (2017) 431–437.

[15] C. Kreischer, T. Volkmann, Transformation kinetics of the metastable bcc phase during rapid solidification of undercooled Fe-Co alloy melts, Materialia 20 (2021) 101211.

[16] C. Kreischer, Crystallization and transformation of metastable phases in undercooled metallic melts, Ph.D. thesis, Technical University of Aachen (RWTH), Aachen, Germany, 2022.

[17] R.E. Cech, Evidence for solidification of a metastable phase in Fe-Ni alloys, JOM 8 (1956) 585–588.

[18] D.J. Thoma, J.H. Perepezko, Microstructural transitions during containerless processing of undercooled Fe-Ni alloys, Metall. Trans. A 23A (1992) 1347–1362.

[19] K. Eckler, F. Gärtner, H. Assadi, A. Norman, A.L. Greer, D.M. Herlach, Phase selection, growth, and interface kinetics in undercooled Fe-Ni melt droplets, Mater. Sci. Eng. A 226-228 (1997) 410–414.

[20] T. Koseki, M.C. Flemings, Solidification of undercooled Fe-Cr-Ni alloys: part I. Thermal behavior, Metall. Mater. Trans. A 26A (1995) 2991–2999.

[21] T. Volkmann, W. Löser, D.M. Herlach, Nucleation and phase selection in undercooled Fe-Cr-Ni melts: part II. Containerless solidification experiments, Metall. Mater. Trans. A 28A (1997) 461–469.

[22] D.M. Matson, Growth competition during double recalescence in Fe-Cr-Ni alloys, MRS Online Proc. Libr. 551 (1998) 227–234.

[23] O. Shuleshova, I. Kaban, W. Löser, S. Ziller, U. Reinhold, D. Lindackers, Metastable phase formation in undercooled Fe-Co melts under terrestrial and microgravity conditions, IFW Dresden, Annu. Rep. (2017) 39–42.

[24] D.M. Matson, X. Xiao, J.E. Rodriguez, J. Lee, R.W. Hyers, O. Shuleshova, I. Kaban, S. Schneider, C. Karrasch, S. Burggraff, R. Wunderlich, H.J. Fecht, Use of thermophysical properties to select and control convection during rapid solidification of steel alloys using electromagnetic levitation on the space station, JOM 69 (2017) 1311–1318.

[25] A.F. Andreoli, O. Shuleshova, V.T. Witusiewicz, Y. Wu, Y. Yang, O. Ivashko, A.C. Dippel, M.v. Zimmermann, K. Nielsch, I. Kaban, *In situ* study of non-equilibrium solidification of CoCrFeNi high-entropy alloy and CrFeNi and CoCrNi ternary suballoys, Acta Mater. 212 (2021) 116880.

[26] T. Degen, M. Sadki, E. Bron, U. König, G. Nénert, The HighScore suite, Powder Diffr. 29 (S2) (2014) S13–S18.

[27] S.N. Kabekkodu, A. Dosen, T.N. Blanton, PDF-5+: a comprehensive powder diffraction File™ for materials characterization, Powder Diffr. 39 (2024) 47–59.

[28] C.A. Schneider, W.S. Rasband, K.W. Eliceiri, NIH Image to ImageJ: 25 years of image analysis, Nat. Methods 9 (2012) 671–675. Software online at: https://imagej.net/ij/.

[29] S. Krishnan, R.H. Hauge, J.L. Margrave, Spectral emissivities and optical constants of electromagnetically levitated liquid metals as functions of temperature and wavelength, in: R.R. Hale (Ed.), Proceedings of the Second Noncontact Temperature Measurement Workshop, Pasadena, CA, USA, 1989, pp. 110–140. Online at: https://ntrs.nasa.gov/citations/19900008591.

[30] J. Kieffer, V. Valls, N. Blanc, C. Hennig, New tools for calibrating diffraction setups, J. Synchrotron Radiat. 27 (2020) 558–566.

[31] T. Nishizawa, K. Ishida, The Co-Fe (cobalt-iron) system, Bull. Alloy Phase Diag. 5 (1984) 250–259.

[32] W.J. Boettinger, U.R. Kattner, K.W. Moon, J.H. Perepezko, NIST recommended practice guide: DTA and heat-flux DSC measurements of alloy melting and freezing, Natl. Inst. Stand. Technol., Spec. Publ. 960-15, Gaithersburg, MD, USA, 2006. DOI: 10.6028/NBS.SP.960-15.

[33] S. Zla, M. Kawuloková, L. Drozdová, B. Smetana, J. Dobrovská, J. Vontorová, P. Váňová, V. Janalíková, Influence of heating rate on the liquidus temperature measured by DTA method for Fe-C-Cr based systems, in: Proceedings of the 26th International Conference on Metallurgy and Materials, Brno, Czech Republic, 2017, 24-26 May. Online at: https://www.confer.cz/metal/2017/1484-influence-of-heating-rate-on-the-liquidus-temperature-measured-by-dta-method-for-fe-c-cr-based-systems.

[34] J.E. Rodriguez, D.M. Matson, Thermodynamic modeling of the solidification path of levitated Fe–Co alloys, CALPHAD: Comput. Coupling Phase Diagrams Thermochem. 49 (2015) 87–100.

[35] T. Kasé. On the equilibrium diagram of the iron-cobalt-nickel system, Science Reports, Tohoku Imperial University, Sendai, Japan, 16, 1927, pp. 491–513.

[36] A.F. Guillermet, Assessing the thermodynamics of the Fe-Co-Ni system using a calphad predictive technique, CALPHAD (1989) 1–22.

[37] A.F. Guillermet, The Fe-Mo (Iron-Molybdenum) system, Bull. Alloy Phase Diag. 3 (1982) 359–367.

[38] A. Davydov, U.R. Kattner, Thermodynamic assessment of the Co-Mo system, J. Phase Equilibr. 20 (1999) 5–16.

[39] S.H. Zhou, Y. Wang, C. Jiang, J.Z. Zhu, L.Q. Chen, Z.K. Liu, First-principles calculations and thermodynamic modeling of the Ni–Mo system, Mater. Sci. Eng. A 397 (2005) 288–296.

[40] S. Wang, X.F. Yao, Y.Q. Su, Y.J. Ma, High temperature image correction in DIC measurement due to thermal radiation, Meas. Sci. Technol. 26 (2015) 095006.

[41] V. Kaban, C. Leyens, J.K. Hufenbach, Non-equilibrium solidification of undercooled Inconel 718, J. Alloy. Compd. 1002 (2024) 175205.

[42] F. Spaepen, A structural model for the solid-liquid interface in monatomic systems, Acta Metall. 23 (1975) 729–743.

[43] F. Spaepen, R.B. Meyer, The surface tension in a structural model for the solid-liquid interface, Scr. Metall. 10 (1976) 257–263.

[44] C.V. Thompson, Crystal formation in easy glass-forming metallic alloys, Ph.D. thesis, Harvard University, Cambridge MA, 1981.

[45] T.F. Kelly, J.B. Vander Sande, Nucleation of alternative crystallization phases, Int. J. Rapid Solidif. 3 (1987) 51–79.

[46] D.M. Matson, Retained free energy as a driving force for phase transformation during rapid solidification of stainless steel alloys in microgravity, npj Microgravity 4 (2018) 22.
[47] D.M. Matson, R.W. Hyers, Adiabatic remelting of the mushy-zone during rapid solidification, Philos. Mag. 86 (2006) 3795–3807.
[48] J.E. Rodriguez, D.M. Matson, Lateral heat flux and remelting during growth into the mushy-zone, Acta Mater. 129 (2017) 408–414.
[49] J.K. Chen, R.A. Vandermeer, W.T. Reynolds, Effects of alloying elements upon austenite decomposition in low-C steels, Metall. Mater. Trans. A 25A (1994) 1367–1379.
[50] H. Oikawa, Lattice diffusion in iron–A review, Tetsu-to-Hagane 68 (1982) 1489–1497. https://www.jstage.jst.go.jp/article/tetsutohagane1955/68/10/68_10_1489/_article/-char/en.
[51] H. Nitta, T. Yamamoto, R. Kanno, K. Takasawa, T. Iida, Y. Yamazaki, S. Ogu, Y. Iijima, Diffusion of molybdenum in α-iron, Acta Mater. 50 (2002) 4117–4125.
[52] W.W. Cias, D.V. Doane, Phase transformational kinetics and hardenability of alloyed medium-carbon steels, Metall. Trans. 4 (1973) 2257–2266.
[53] H.I. Aaronson, W.T. Reynolds, G.R. Purdy, Coupled-solute drag effects on ferrite formation in Fe-C-X systems, Metall. Mater. Trans. A 35A (2004) 1187–1210.
[54] G. Miyamoto, K. Yokoyama, T. Furuhara, Quantitative analysis of Mo solute drag effect on ferrite and bainite transformations in Fe-0.4C-0.5Mo alloy, Acta Mater. 177 (2019) 187–197.
[55] P. Uranga, C.J. Shang, T. Senuma, J.R. Yang, A.M. Guo, H. Mohrbacher, Molybdenum alloying in high-performance flat-rolled steels grades, Adv. Manuf. 8 (2020) 15–34.
[56] S. Kajiwara, Role of dislocations and grain boundaries in martensite nucleation, Metall. Trans. A 17A (1986) 1693–1702.
[57] D. Farache, S. Mishra, S. Tripathi, A. Strachan, Role of dislocations on martensitic transformation temperatures and microstructure: a molecular dynamics study, J. Appl. Phys. 136 (2024) 035106.